

Paul V. Gwozdz, Jann Harberts, Robert Zierold and Robert H. Blick*

Label-free single-cell counting and characterization in the GHz-range

<https://doi.org/10.1515/freq-2022-0132>

Received June 24, 2022; accepted October 6, 2022;

published online October 20, 2022

Abstract: We demonstrate operation of a micropore based flow cytometer in the radio-frequency range. Apart from simply counting micron sized particles, such as cells, with close to nano-second resolution this counter offers the additional benefit of delivering insight into the intracellular environment. Such non-invasive screening of the cell's interior based on analysing amplitude and phase of the signal is helpful in characterizing the biological activity of cells. In detail we are using heterodyne mixing to demodulate the temporal impedance changes, which are induced by cells translocating through a micropore embedded in a radio-frequency circuit. This allows us to measure every amplitude and phase modulation induced by a translocation event. Herein, we compare the Jurkat cells (human T lymphocytes) recordings with a control group of polystyrene beads. As the cells are measured on a single cell level, the variations on the measured amplitude and phase signals are used, herein, to sense morphological cell changes in real time.

Keywords: radio frequency circuits; single cell counting; spectroscopic probing.

1 Introduction

Dielectric spectroscopy of biological materials is a method pioneered by Schwan and Foster [1]. Over the years, they recorded the electronic response of biological tissue exposed to electromagnetic fields, revealing a particular frequency signature [2–4]. The overall conclusion was that

tissue, which is exposed to electromagnetic fields in the kHz-region, exhibits a low conductivity σ and an extremely high dielectric constant ϵ , combined with a characteristic low-frequency dispersion, related to the poorly conducting cell membranes [5]. Increasing the frequency to 10 MHz and above leads to a second dispersion, which is most likely caused by the membrane structure of the biological tissue, theoretically described by the Maxwell-Wagner effect [6]. In detail, this is related to the presence of a highly conductive cell interior surrounded by a poorly conducting cell membrane resulting in a distinct variation in the dielectric response [7]. At high frequencies of 100 MHz to several GHz, however, the membrane, which is in a first approximation a nonconductive entity separating two fluidic compartments, is electrically shorted out such that the AC field is reaching through the cell membrane. Thus, the measurement becomes sensitive to the intracellular medium [8]. These three distinct dispersion regions are commonly labeled as α -, β -, and γ -dispersions and were summarized by Gabriel et al. for a variety of different tissues [9]. They showed that although the overall frequency dependent dielectric permittivity and electrical conductivity varies depending on the type of tissue, the general division into these three regions remains.

On the tissue level it was shown e.g. that the dielectric properties change in malignant liver tissue [10, 11], lung tissue [12, 13], in oral cancer cells [14], breast cells [13], to name only some examples. Nevertheless, the main drawback of the majority of experiments is the fact that the dielectric response is measured using an open coaxial probe, which is brought into direct contact with the tissue under investigation. This tissue sample is typically macroscopic and thus the measurement result intrinsically reflects on an average over the measured sample. As biological matter can potentially be extremely heterogeneous, measuring the dielectric properties of single cells is in general favorable [15].

The first approaches into measuring single cells translocating through micro-channels and passing between in-plane electrodes was undertaken by Ayliffe in 1999 [16]. They were able to show that red blood cells and granulocytes reveal different amplitude and phase signals at frequencies up to 2 MHz. A high speed measurement setup based on a planar coplanar waveguide (CPW)

*Corresponding author: Robert H. Blick, Center for Hybrid Nanostructures (CHyN), Universität Hamburg, DESY Campus Bldg. 600, Luruper Chaussee 149, 22761 Hamburg, Germany; and Materials Science and Engineering, University of Wisconsin-Madison, 1550 University Avenue, Madison, WI, USA, E-mail: rblick@chyn.uni-hamburg.de

Paul V. Gwozdz, Jann Harberts and Robert Zierold, Center for Hybrid Nanostructures (CHyN), Universität Hamburg, DESY Campus Bldg. 600, Luruper Chaussee 149, 22761 Hamburg, Germany

structure was then demonstrated by Wood et al. [17], who demonstrated sensitive detection of single particles translocating over a conventional co-planar waveguide (CPW) in conjunction with a microfluidic channel, operating at a radio-frequency (RF) of 170 MHz. Later this sensor was further optimized in terms of sensitivity by using two parallel electrodes within a microfluidic channel operating at 100 MHz [18].

Based on recent progress in micro-electronic and – fluidic device technology [19–21], in conjunction with RF-circuits [22–25] dielectric spectroscopy now holds huge potential as a noninvasive and label free characterization method for single cells [26, 27]. An advanced approach based on tubular CPWs (T-CPWs), was demonstrated by Bausch et al. Here, the tubular CPW was employed for T cell counting, enabling enhanced detection sensitivity in the radio-frequency range at 177 MHz [28].

All the device configurations mentioned above come with their advantages and disadvantages: the major drawback lies mostly in the complex and costly fabrication and the often limited frequency range. Here, we present a device, which overcomes most of these issues. It consists of a CPW integrated on borosilicate glass slides. A micropore (MP) is drilled directly into the glass by laser ablation from a high-powered ArF excimer lasers [29, 30]. This preparation method allows for rapid and inexpensive yet reliable preparation of the CPW-chip for microwave cell analysis. The actual chip design for the RF-range we tested in our earlier device, which established the measurement strategy [31]. Since our pore drilling can be tuned in order to obtain pore diameters in the range from 1 to 10 μm and more, we can precisely adjust it to the diameter of the cells under test (CUT). As the characterization of Jurkat cells is the focus of this work, we are showing high-frequency recordings with 11 μm MP diameter on average. The MP is embedded between the open end of the signal line of the CPW and an adjacent ground metallization (see Figure 1). Consequently, the application of an RF-field to the CPW leads to a strong electric field gradient in the plane close to the MP. Particles or cells, which translocate the MP due to an applied suction, strongly interact with the electrical field at the open end of the CPW. Consequently, the interaction between cells and electromagnetic field, alters the RF-signal's reflection. In detail, we make use of amplitude and phase of this reflected RF-wave to characterize the individual cells. The chip is designed to operate at frequencies 700 MHz. Hence, the device is most prominently sensitive to the intercellular medium of the tested cells. By purposefully altering the suspension of the CUTs (Jurkat cells) from a physiological into a

non-physiological buffer, we are able to induce and *in-situ* detect apoptosis of the cells. This in turn, we are able to trace amplitude and phase change of the reflected signal for different physiological conditions of the cells.

2 Materials and methods

A schematic of the integrated micro/electronic-fluidic RF-chip is shown in Figure 1. It consists of a borosilicate glass slide with a thickness of nominally 170 μm and lateral dimensions of $24 \times 50 \text{ mm}^2$. Using optical lithography the top of the glass slide is patterned with a CPW (Figure 1a). The RF-input port is transitioning to a thin signal line (width of 75 μm), which has a constant gap of 50 μm to the ground metallization. The signal line has a total length of 3.4 cm, which determines the resonance frequency. For the metallization of the CPW, Au-layers with a thickness of 110 nm are thermally evaporated on top of a 10 nm Cr-adhesion layer.

The signal line, on which the RF-wave is traveling to the sensing region, has an open end at which a MP is located, as illustrated in Figure 1b and c. The MP is embedded between the open end of the signal line and a bulge in the ground metallization thus defining the signal region of the chip. It is necessary to isolate most of the signal line from the electrolyte solution in which the cells are suspended. Otherwise the RF-signal would be strongly attenuated. Therefore, the area around the signal region is covered with a thick (200 μm) layer of the positive photoresist SU-8, which is isolating the signal region from the liquid but exposing the MP. In this way a negative pressure can be applied from the backside of the chip to induce particle translocation through the MP. Furthermore, it can be seen in Figure 1b that the ground metallization is moved out forming a half-bowtie shape. Such a geometry reduces fringing fields at the sensing region thus focusing the localized electrical field between the open end of the signal line and the ground metallization.

The MP is drilled into the glass substrate after the lithographic steps used for patterning the CPW and the SU-8 fluidic chamber. We then employ direct laser ablation by an ArF excimer laser from the backside of the glass chip leading to conical pores with tunable pore diameters at the signal region. This process was discussed before and also in recent work [29, 30], which describes the drilling process in detail. In the current case, the parameters of the drilling process are adjusted in such a way that an MP with an open diameter of 11 μm is produced. The pore is drilled from the backside of the RF-chip. Due to the limited resolution of the sample stage for direct-laser-writing, the MP currently can only be positioned with an accuracy of about 2 μm with respect to the gap between the signal line and the ground metallization. In order to position the MP in-between the electrodes the signal region further processed using focused ion beam (FIB) milling and FIB induced metal deposition [32]. A schematic of the resulting FIB deposition process is given in Figure 1c. For the FIB induced metal deposition, the Au-layer in the vicinity of the MP is milled away with the Ga-source of the FIB. The next step consists of depositing Pt-electrodes locally, patterned in such a way that their tips have direct contact with the MP. Importantly, this FIB post-processing step allows for precise reproduction of the MP-antenna configuration, showing the signal line and ground in yellow and the local Pt-electrodes in orange. This procedure leads to an optimized sampling configuration for RF-measurements, as shown in Figure 1d.

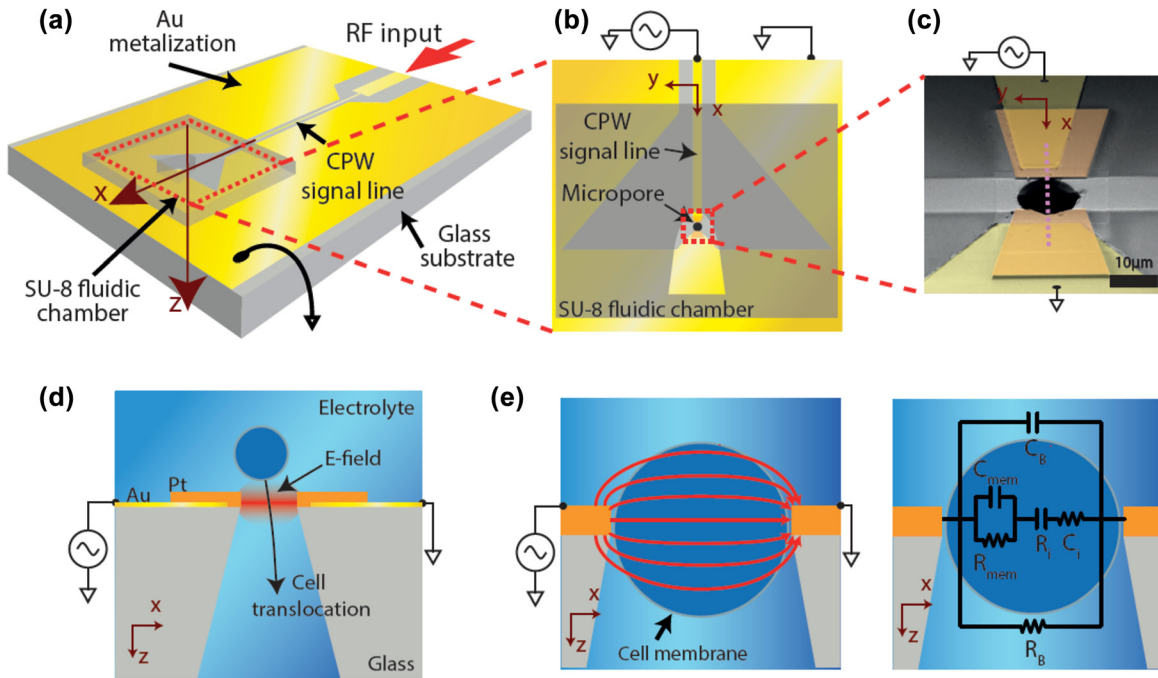


Figure 1: In this Figure we show the overall experimental configuration. (a) Schematic of the glass based RF chip. The glass has a thickness of 170 μm with an Au-coplanar wave guide (CPW) patterned on top. The micro-pore (MP) is located at the open end of the CPW signal line and the signal region around the MP is isolated from the electrolyte solution with a 200 μm SU-8 based fluidic channel. (b) Top view onto the signal region. The ground metallization is moved out thus reducing fringing fields at the signal region. (c) SEM image of the sensing region. In yellow the Au-metallization is shown and in orange the Pt-electrodes that are patterned with a focused ion beam unit induced Pt-deposition. The region between the electrodes is milled away with the FIB to prevent a short circuit between the signal line and the ground. (d) Side-view through the MP. Thick Pt-electrodes are patterned locally at the vicinity of the MP producing a strong electrical RF field across the MP. Cells suspension is pipetted onto the signal region and cell translocation is induced by an applied suction. Illustration of the electrical field between the signal line and the ground metallization (left) and an equivalent circuit model of a translocating cell. (e) Field line representation and lumped element circuit model of the actual sensing circuit.

Finally, the glass chip is soldered on a custom-made printed circuit board (PCB), which connects to two SMA-ports. One connector is used to guide the RF-wave into the chip and the second connector is utilized to apply a constant voltage across a tunable varactor diode of the matching circuit. This varactor is used to tune the impedance of the chip to the standard 50 Ω transmission line impedance to which the chip is connected. Underneath the glass chip a drilled-out screw cap is glued in such a way that a pump can be interfaced with the chip. This facilitates suction control for inducing particle translocations through the MP.

For the current cell measurements the RF is fixed just below 1 GHz at around 700 MHz. At this frequency the impedance of cell membranes is substantially lowered, since the membrane acts mostly like a capacitor with a capacitance C_m and a resistance of R_m . Thus, the RF-field penetrates through the cell membrane, as schematically shown in Figure 1e. Consequently, our measurement is sensitive to the cytoplasm of the individual cells. The interaction of the cell and the electrical field in the sensing region leads to an amplitude modulation (AM) of the 700 MHz carrier wave. A reflection measurement is performed to trace this AM. In addition the inset of the right-hand-side part of Figure 1e gives a lumped element circuit diagram in which the contribution of the cells resistance and capacitance are noted. Directly sampling of such frequency signals is experimentally difficult and absolute values of resistance and capacitance depend on the frequency of operation. Fortunately, the translocation time of

particles with diameters in the micron range is fairly slow with some ms. Hence, a down-conversion of the frequency is sufficient. Here, we use a heterodyne mixing setup to down-convert the RF-signal to a frequency of 100 MHz, while maintaining amplitude and phase of the signal [33].

The final measurement of the reflected signal is performed with a high-speed lock-in amplifier. A schematic of this modulation procedure is shown in Figure 2. The core of the heterodyne receiver is the mixer, which is used for the down-conversion. A synthesizer is used to produce the RF-wave, which is relayed to the MP-chip. Particles that translocate the signal region perturb the electrical field and thus change the overall impedance of the chip. This is measured as an AM of the reflected wave. The induced amplitude modulation is carried on the reflected RF-wave. This signal is fed to the frequency mixer. A second signal generator is providing the local oscillator (LO) reference. This LO has a fixed frequency difference from the RF wave. As a consequence the intermediate frequency (IF) output of the mixer contains the product of the two waves with frequency components $f_{IF} = f_{RF} \pm f_{LO}$.

For the current experiments presented here a frequency difference of 100 MHz was chosen for best phase noise performance while maintaining temporal resolution. Therefore the $f_{RF} + f_{IF}$ component has a frequency of $f_{IF} = 2f_{RF} + 100 \text{ MHz}$ and the $f_{RF} - f_{IF}$ component has a frequency of $f_{IF} = 100 \text{ MHz}$. The resulting signal is measured with a lock-in amplifier (Zurich Instruments UHFLI), which can process

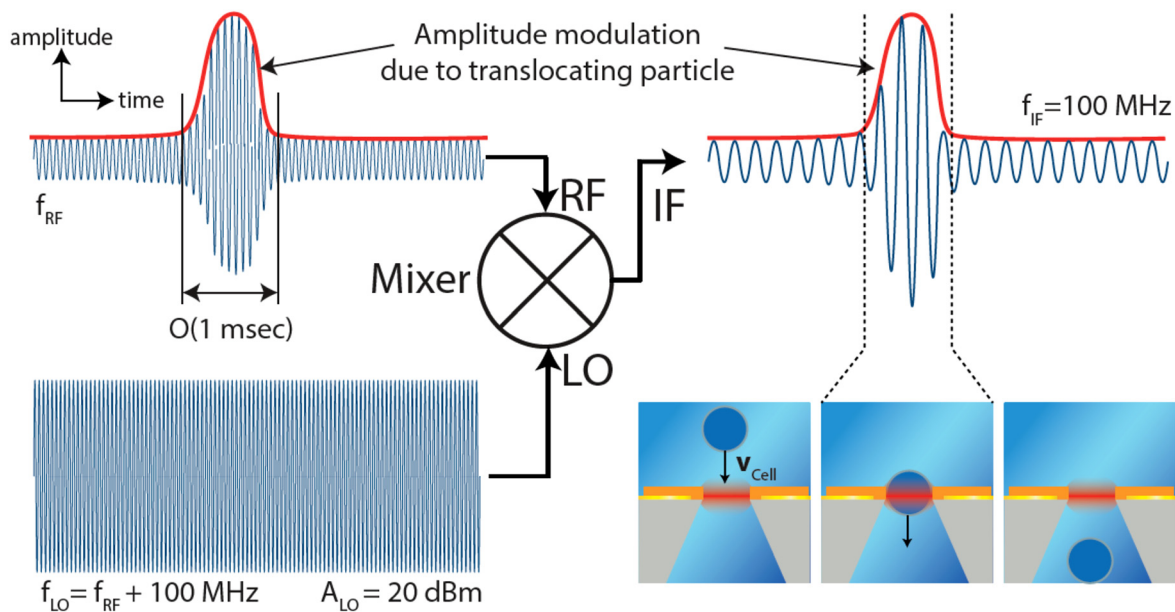


Figure 2: Schematic of heterodyne mixing: a translocating cell produces an amplitude modulation of the carrier wave having a frequency in the RF-range of 700–1000 MHz. The amplitude of the reflected signal is modulated (red envelope) and also the phase. The RF-signal is down-converted using a mixer that uses a local oscillator (LO) wave to produce the intermediate frequency (IF). For sensing the low-frequency signal the IF term is processed, delivering an amplitude and phase signal.

frequencies as high as 600 MHz. Due to this bandwidth (BW) limitation of the lock-in input, the high frequency component of the mixing process is filtered out and the measured signal is an AM carrier wave at 100 MHz. At this frequency the AM input can be directly demodulated by the lock-in using the internal signal generator as a reference, which is phase-locked to the IF-signal. As the heterodyne mixing not only preserves the amplitude modulation, but as well the phase of the signal, a translocating particle can be characterized by three measurement quantities; the amplitude of the reflected signal, the phase change, and the translocation time in the following referred as such.

Before particle translocation can be measured, the RF-chip has to be impedance matched to the standard 50 Ω transmission line (TL) setup. This process of impedance matching was already described elsewhere [31]. As mentioned previously the impedance matching circuit that is mounted on the PCB consists of a tunable varactor diode in series with the signal line. In series to the varactor two surface mount capacitors are located, which block any potential direct currents to reach the signal source or the signal region of the RF-chip. To block any RF-signals reaching the DC source two high-ohmic resistors are connected in parallel to the varactor diode.

The circuit allows tuning the impedance of the overall chip to the 50 Ω TL to which the chip is connected. It is well known that in RF circuits any mismatch in impedance between the source and a load leads to a reflection of the RF wave back into the source [34, 35]. To prevent that the load has to be impedance matched in such a way that the reflection at the frequency of operation is minimized according to $\Gamma = (Z_L - Z_0)/(Z_L + Z_0)$. A DC-voltage applied to the varactor diode allows for tuning Z_C , in such a way that at a certain RF the chip impedance is similar to Z_0 . Consequently the RF-energy, reaching the half bow-tie antenna region, is absorbed by the circuit. In Figure 1d side-view of the MP together with the in plane metal electrodes is

shown. Cells suspended in electrolyte translocate through the MP and thus pass the in-plane electrodes. If the device is impedance matched a strong RF-field is generated between the electrodes, which is illustrated in the left plot of Figure 1e. The cell can be described electrically using the schematic shown in the right plot in Figure 1e.

Results from the impedance matching are given in Figure 3a and b: in (a) the reflection of a typical RF-chip is given versus the input frequency and the varactor voltage for a dry chip (i.e. without electrolyte solution only within the sensing volume, but not the leads). At a certain combination of RF and varactor voltage the reflection shows a minimum, which is the point of optimal impedance matching. A cut through this point is given for the frequency and voltage sweep, as a black solid and dashed line in Figure 3b. The reflection response for a detuned chip is shown in the figure. Obviously, for a detuned device a portion of the incoming wave is reflected back without reaching the signal region.

In Figure 3c and d the power spectral density (PSD) of a time domain signal is given for an impedance matched (black) and a detuned chip is given. It is obvious that for an impedance matched chip the PSD is flat up to frequencies of 1 MHz. Consequently, for the time domain measurement, an increased measurement BW will lead to a linear noise contribution because of an absence of high frequency noise. This is in contrast to corresponding pore-based resistive pulse measurements, which typically show dielectric and capacitive noise contributions that fundamentally limit the BW of such measurements [36, 37]. Another feature of the PSD is the fact that a detuned chip does show an increased low frequency noise contribution. It will be discussed later in the text that this leads to an increased baseline amplitude without introducing any high frequency noise.

In Figure 4a and b the results of the measured demodulated amplitude and phase of the reflected RF-signal are shown: the peaks in the time traces are originating from individually translocating

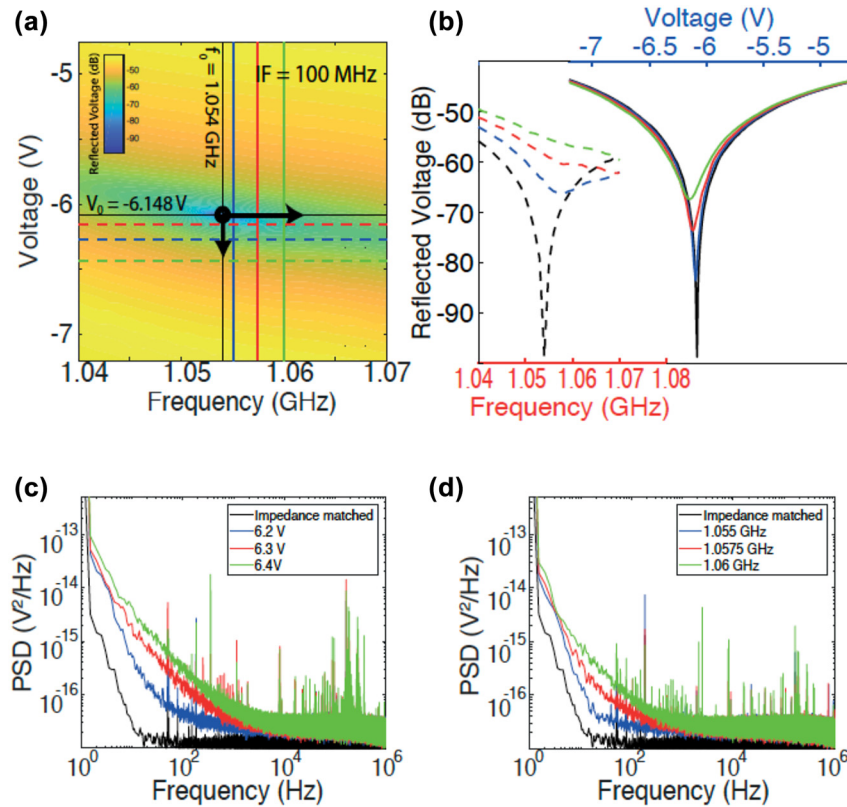


Figure 3: Characterization of the overall circuit. (a) Impedance matching of the RF-chip at fixed RF frequency just above 1 GHz. This resonance frequency typically drops when the complete microfluidic channel for feeding the cell suspension is connection. (b) Reflection measurements for different varactor voltages and input frequencies showing that the quality of the match decreases with values different from f_0 and V_0 . This demonstrates how the tuning is performed during cell measurements. (c, d) Power spectral density for the investigated tuning range of drive frequency f_0 and varactor voltage V_0 . The noise is strongly reduced for the final range of operation at just below 1000 MHz.

Jurkat cells. In (a) the amplitude of the reflected signal is shown together with a zoomed-in view into one individual translocation event. The baseline amplitude is set to about 0.5 mV which is achieved by detuning the RF-chip intentionally due to a change of the varactor voltage until the desired baseline amplitude is reached. Such detuning does not compromise the signal amplitude, as we have tested by measuring the amplitude of the reflected signal versus the baseline signal. In the lower plot in (a) the corresponding phase change is shown. Every amplitude modulation is accompanied by a characteristic phase change. Without a particle in the MP the phase signal is centered around zero. A translocating particle first increases the phase to positive angles. When the particle exists the sensing region the phase change makes one characteristic negative phase change before reaching zero again. A combined close-up view of a single event is shown in Figure 4b, where the resonator behavior is clearly visible. Note, the characteristic shape of the phase trace upon a translocation event, can be utilized to clearly identify such a signal from noise or other disturbing signals during measurement. We note that we measure the resonating tank circuit in a fashion in which amplitude and phase modulation of the resonator are traced in the time domain.

For the analysis of this data a moving average is applied to the reflected amplitude to produce an estimate for the baseline signal without the cells' signals. The window in which the average is evaluated is chosen in such a way that the time evolution of the signal is reproduced by simultaneously rejecting the modulation due to the translocating cells. The moving average (displayed in the upper plot in Figure 4a as a red trace) is subtracted from the raw data, thus leading to a baseline amplitude centered around zero. In this situation a peak finding algorithm is applied, which is detecting the

individual translocation events if they exceed a threshold value of 3σ of the moving standard deviation. In this manner the position and amplitude of the transient peaks are determined. Based on the position of the transient AM, the position of the first positive phase peak is determined. This first phase peak coincides with the position of the amplitude peak. Finally, the peak finding algorithm is used to determine the following negative phase peak. In summary three quantities can be deduced from one translocation event namely the amplitude, phase, and the width of the event (see Figure 4c). The biophysical implications will be discussed in the following section.

It was already mentioned that the baseline amplitude of the reflected signal is intentionally set to 0.5 mV by detuning the varactor voltage away from the point of optimal impedance match. This is necessary because in the presented configuration the lock-in amplifier is not capable to phase-lock the reflected signal, if the input amplitude is too low. In the PSD discussed in Figure 3c and d it was shown that such a detuning increases low-frequency noise, but does not compromise the high frequency noise. Hence, a detuned RF-chip leads to a lower reflected mean amplitude of the individual translocating particles. This is shown in Figure 4c. For a number of translocating T cells the mean amplitude is measured. The results of these measurements are repeated for different detuning values. Experimentally it is challenging to reach stable reflected amplitudes that are very small. Interestingly the mean reflected amplitudes are not the highest for the best impedance match but the highest value is measured at about 0.3 mV baseline amplitude. Above this value the mean amplitude decreases. For the following experiments a mean amplitude of 0.5 mV is chosen because this gave the best compromise between a stable phase measurement and the highest mean signal amplitude.

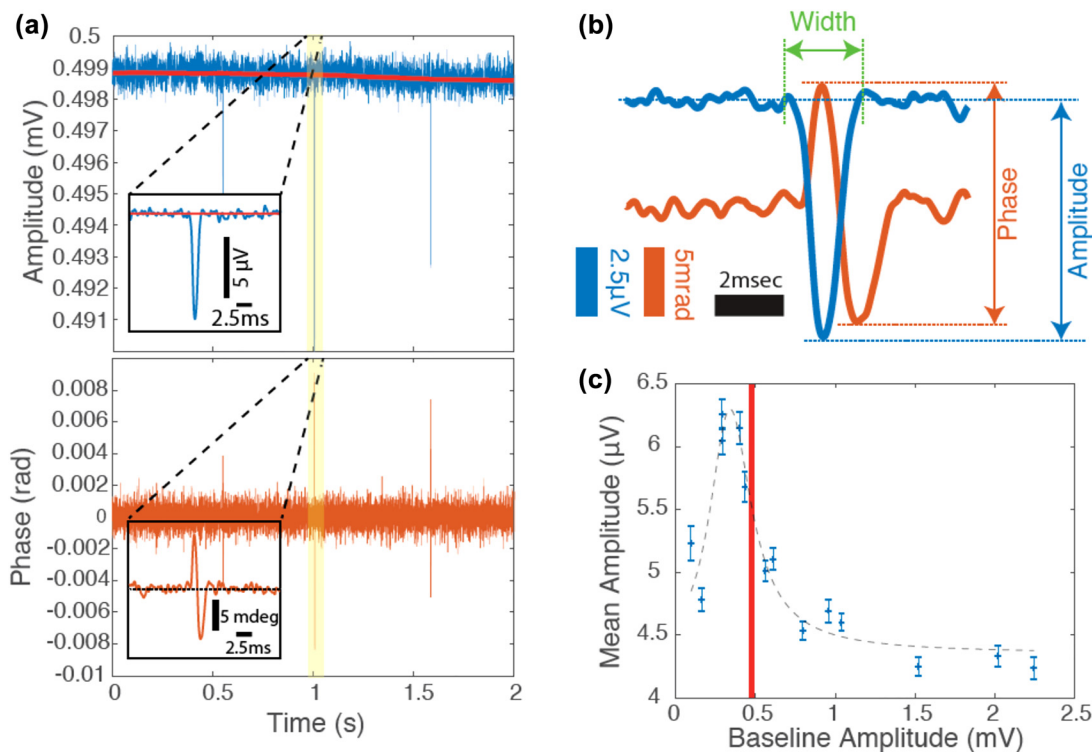


Figure 4: Typical data trace and detailed analysis. (a) Measured time domain recording of the reflected amplitude (top) and phase (bottom) modulation due to the translocation of individual Jurkat cells through the micro-pore. An exemplary translocating event is highlighted in yellow and also shown in the inset. (b) Direct comparison of amplitude and phase signals from a single translocation event. Clearly the synchronization of amplitude and phase is seen, which is then used to numerically extract translocation events from the data. (c) Mean peak amplitude from translocating T cells versus mean baseline amplitude which is adjusted by the value of the varactor voltage.

Three electrolytes are used for the measurement experiments. Particles that are measured in the flow cytometer are polystyrene beads with a diameter of 6 μm and Jurkat cells. On the one hand, the beads are diluted in the desired buffer solution to a concentration of about $10^6/\text{mL}$. This concentration is a compromise between a reasonable event rate and the time it is possible to measure before the MP could clog up. On the other hand, Jurkat cells are kept in culture in RPMI 1640 medium with 7.5% newborn calf serum and 1.2% penicillin/streptomycin. They are incubated at 37 °C at 5% CO_2 . Under these conditions the cells are diluted every second day, except of the weekend thus keeping the concentration of the cells constant. For the experiments the cells are finally transferred into a measurement buffer. Note, different buffers are used but the process of transferring is always the same. 5 mL of the cell culture is centrifuged for 5 min at 2000 rpm (1000g). The medium is decanted from the resulting cell pellet and the desired buffer is given to the pellet and the cells are gently re-dispersed, to wash the cells. A second similar centrifugation step follows and the buffer is decanted again. Finally, fresh buffer is added to the cell pellet and the re-dispersed sample is ready for the RF measurement.

3 Results and discussion

Our RF device is first tested for operation with polystyrene beads with a diameter of 6 μm. In a second step we

make use of the T cells, which are suspended in a physiological Ca^{2+} measurement buffer. Additionally, a part of this cell batch is transferred into another buffer, which is purposefully non-physiological. The main difference between this buffer and the Ca^{2+} -buffer is the salt concentration. On the one hand, a physiological Ca^{2+} -buffer contains mostly NaCl at 140 mM. On the other hand, the pipette solution, which is used in standard patch clamp experiments as the buffer inside the patch pipette thus mimicking the intraellular environment [38, 39], contains mostly KCl at 140 mM. However, such an electrolyte outside the cell is not physiological and results in a change of the electrophysiological state of the cell and could finally lead to cell death, which – as it turns out – can be sensed with the RF-chip.

Results from the three experiments are shown in Figure 5: we are comparing (i) polystyrene beads (blue circles and traces) with (ii) T cells in physiological solution (PS) purple and (iii) T cells in non-physiological solution (NPS) as red circles. All of these have been measured in a circuit impedance matched to the pipette solution (NPS). Empty, light colored circles show the same measurements but impedance matched to the Ca^{2+} buffer

(PS). Shown are the histograms of the measured amplitude, phase degree, and the duration of translocation, the width, as selected line plots in (a–c). The scatter plots in (d–f) beneath are relating these three properties. Note, the impedance match variation between the PS and NPS is only marginal.

In Figure 5a we plot the normalized histogram of translocation events under pressure driven flow (PDF) versus peak amplitude of the translocating particles. As seen most of the polystyrene beads (blue) induce small amplitude signals within the range of 1–2 μV . A very similar response is found with the intact T cells from the PS (deep purple) pass through the MP. Again, we find a spike around 1–2 μV , which trails off towards 5 μV . Hence, we can conclude that the spherical character of these T cells is well maintained. This behavior can be explained by the fact that the sensing electrodes are on the topside of the MP (see Figure 1d). The spherical particles, both beads and T cells, approach the sensing region and capacitively induce voltage spikes in the electrodes. The maximal signal is obtained when these ‘spheres’ are in between the MP-electrodes (see Figure 1e). Based on this data we would expect a slightly larger peak value for the T cells as

compared to the beads, due to the larger radius. However, since also the dielectric constant contributes to the reflected signal amplitude, different sizes can give the same measured amplitude. The different sizes and size distributions of bead and cells can be identified in Figure 5c by the narrower PDF distribution shifted to shorter times for beads. When we now compare the signal amplitude of the T cells suspended in NPS (red) [40], we find that this signal shows a much larger amplitude response in the range of 6–11 μV , which, at the same time, reveals a very broad distribution. An explanation for this very different response compared to cell in PS might be that the T cells are basically drained off of their intra-cellular fluid in NPS. Thus, the dielectric properties of these T cells are strongly altered and hence their interaction strength with the MP-electrodes changes accordingly. Note, since the signal width remains similar for cells in PS and NPS, we conclude that the shape and the mechanical properties of the cell membrane remain constant leading to equal translocation velocities.

The change of the dielectric properties of the T cells in NPS compared to PS is also found when plotting the normalized histogram of the phase signal, shown in

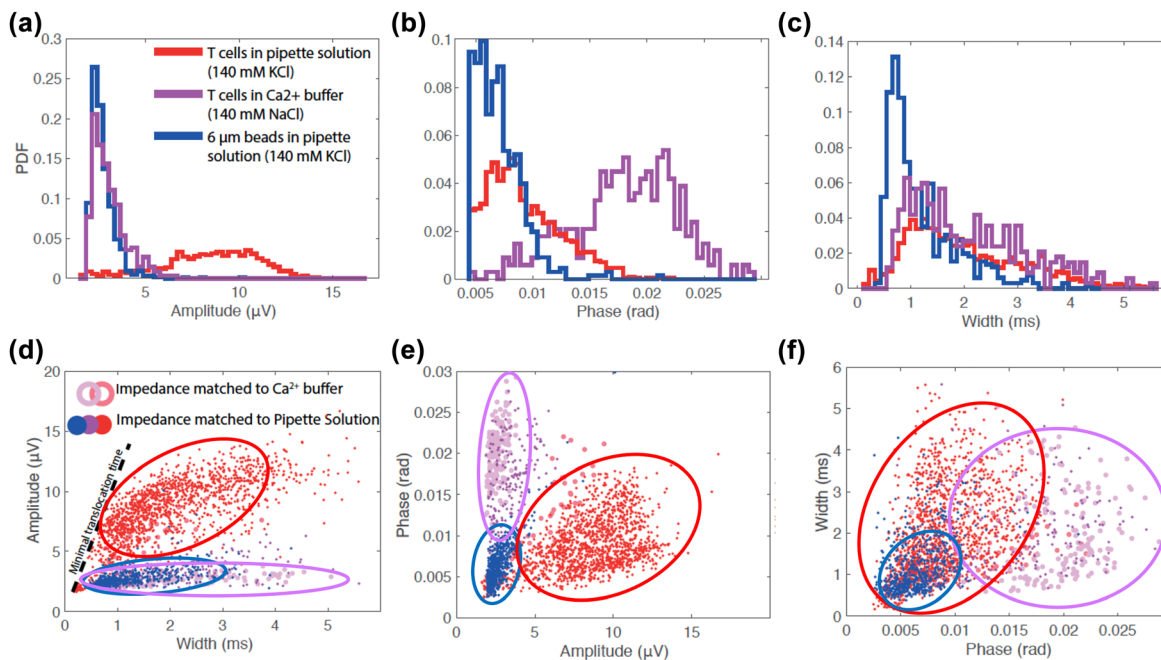


Figure 5: Overall evaluation of applying the circuit for comparative cell analysis. (a) Histogram of pressure driven flow (PDF) of the amplitude of translocation events for polystyrene beads (blue), T cells in physiological solution (deep purple), and T cells in non-physiological solution (red). (b, c) Similar histograms for phase signal and temporal peak width for all three particle classes. (d) Amplitude of reflected signal versus phase shift of polystyrene beads (blue) and T cells suspended in Ca^{2+} -buffer (deep purple) and T cells suspended in pipette solution (red). (e, f) Corresponding scatterplots for the phase versus temporal width of the translocation and width versus amplitude, respectively. As the measurements are performed in different electrolyte solutions the point of optimal impedance is slightly altered when the liquid is interchanged. Open pink and light purple circles represent events when the device is impedance matched to the Ca^{2+} -buffer, while red, blue, and deep purple solid circles represent measurements taken with a device which is impedance matched to non-physiological pipette solution.

Figure 5b. Here the polystyrene beads again show a clear peak with an exponential decay with minimal phase shift. This implies that we find absorption and a certain damping of the electromagnetic signal. The signal of polystyrene beads is very similar to the response of the T cells in NPS. While the peak, i.e. count, is not as pronounced as the featureless yet dense beads, we find a similar behavior, however, with a prolonged decay to about double of the phase lag. This observation can be interpreted as a similar absorption of the electromagnetic radiation inside these T cells. Thus, the expected apoptotic picture by exchange of the electrolyte is corroborated, which implies that these T cells lose their intracellular fluid and behave in that sense a bit similar to dense polystyrene beads. Directly compared to the previous two the T cells in PS (purple trace), however, show a long delayed broad peak in the phase signal. This spread in phase lag is a clear indication of a dispersive process within the T cells in an appropriate environment. In light of the fact that these T cells still contain the intracellular liquid and thus are still ‘alive’, we can assume that we observe the γ -dispersion of single T cells [5]. In other words, we are able to monitor signals from the cells’ interiors by employing an RF-signal resonance signal at 700 MHz and above.

Finally, we can compare the propagation time of the beads and T cells by simply looking at the widths of the resonances, shown in Figure 5c. Here the control beads clearly lead the way, since they fit easily through the MP and do not tend to clog it. Interestingly, the T cells in PS as well as in NPS show a very similar behavior. Hence, one can conclude that these cells have comparable diameters and still show the same mechanical properties since the cells have to gently be squeezed through the MP.

In order to further clarify the T cell recordings we now summarize the histograms in scatter plots in Figure 5d–f: here the three individual quantities amplitude, phase, and width are compared to each other. At first we chose to plot of amplitude versus temporal width of the beads and the different T cells (see Figure 5d). As an additional control we also include in the scatter plots the T cell data where the entire circuit is actually matched to the Ca^{2+} -buffer for both the T cells in PS (light purple rings) and in NPS (light red rings). This representation including all the data is very revealing in a way that we can now clearly discern apoptotic or electro-physiologically altered from live T cells.

A first observation that can be made is that there is a minimal translocation time, which correlates linearly with the amplitude. This minimal translocation time is marked with a dashed black line. The bigger the amplitude the longer the cells tend to dwell in the sensing region.

This result can be explained by the fact that the amplitude is partially a function of the size of the translocating particle. As most of the cells are bigger than the MP it is expected that they will need to squeeze through the pore while having mechanical contact with the pore walls. The bigger the cells are, the bigger the reflected amplitude and consequently the more mechanical contact, slowing down the cell during translocation. At a critical amplitude the linear correlation disappears. While the data for the T cells in PS (deep and light purple) are clustered close to the polystyrene beads (see purple and blue corrals), the T cells in NPS (red and light red) are found in a broad distribution in the center of the graph (red corral). We conclude, that this is a clear indication that our RF-enhanced MPs can be employed as an ultra-high speed cell counter *and* have potential to deliver additional information on the actual physiological status of cells. The strong variation from healthy (purple corral) to dying (red corral) is most likely due to the disintegration of the cells in read-out process. We assume that this is causing the massive increase in amplitude, since the data scatter over a much larger area.

If we now plot the phase signal versus amplitude in Figure 5e we can see an even clearer distinction of T cells in PS (purple corral) and in NPS (red) and the beads (blue). Even for the Ca^{2+} -buffer with a slightly tuned impedance match, we find a similar response (compare light and deep purple data points). In contrast to the amplitude versus width data, however, this plot gives even more physical insight, since we can distinguish all different particle types from each other. This is simply due to the fact that the phase signal in the RF-range above 100 MHz enables to probe the dielectric properties of the particle in addition to simply its size. As before in Figure 5d we can also infer that the T cells in NPS must have gone through an internal structural change during measurement, which is simply seen in the size of the red area circle.

The analysis is completed in Figure 5f where we finally plot the temporal signal width versus the phase signal. Also, here we find three distinct clustering regions as indicated. While the polystyrene beads appear to travel fast without much dispersion, a clear dispersive feature is found for the T cells with the T cells in NPS showing the largest phase lag.

4 Conclusions

We found that our RF-device allows for tracing the translocation of Jurkat cells and polystyrene beads in conjunction with delivering crucial information of the

intrinsic properties of the particles. A slight detuning of the RF-chip allows us to measure not only the temporally modulated amplitude of the reflected signal but also the simultaneous phase changes that are caused by the translocating particles. In detail, cells that are measured in a physiological buffer show a stable correlation between amplitude and the phase. In contrast for cells suspended in non-physiological buffer, we find significant changes in amplitude and phase during the experiment, which can be traced over time. As a consequence, the electrophysiological state of individual cells can be monitored *in-situ*. Hence, our device might pave the way to novel studies of (induced) apoptosis, drug effects, and kinetics of intracellular changes, to name a few.

Acknowledgments: We like to thank our colleagues A. Guse, B. Diercks, and L. Hernandez for in depth discussions and are looking forward to applying our improved devices for detailed studies on T cells.

Author contributions: All the authors have accepted responsibility for the entire content of this submitted manuscript and approved submission.

Research funding: We acknowledge support by the Deutsche Forschungs-gemeinschaft (DFG) within the Priority Program SPP-1857 ('ESSENCE') and by the Joachim-Herz-Stiftung within the 'BioPict'-program.

Conflict of interest statement: The authors declare no conflicts of interest regarding this article.

References

- [1] H. P. Schwan and K. R. Foster, "RF-field interactions with biological systems: electrical properties and biophysical mechanisms," *Proc. IEEE*, vol. 68, p. 104, 1980.
- [2] B. Onaral, H. H. Sun, and H. P. Schwan, "Electrical properties of bioelectrodes," *IEEE Trans. Biomed. Eng.*, vol. 31, pp. 827–832, 1984.
- [3] K. R. Foster and H. P. Schwan, "Dielectric properties of tissue and biological materials: a critical review," *Crit. Rev. Biomed. Eng.*, vol. 17, pp. 25–104, 1989.
- [4] H. P. Schwan, "Linear and nonlinear electrode polarization and biological materials," *Ann. Biomed. Eng.*, vol. 20, p. 269, 1992.
- [5] H. P. Schwan, E. T. McAdams, and J. Jossinet, "Sauer's non-linear voltage division," *Med. Bio. Eng. Comp.*, vol. 40, pp. 542–545, 2002.
- [6] S. Takashima, K. Asami, and Y. Takahashi, "Frequency domain studies of impedance characteristics of biological cells using micropipet technique," *Biophys. J.*, vol. 54, pp. 995–1000, 1988.
- [7] M. Stubbe and J. Gimsa, "Maxwell's mixing equation revisited: characteristic impedance equations for ellipsoidal cells," *Biophys. J.*, vol. 109, p. 194, 2015.
- [8] B. Brazey, J. Cottet, A. Bolopion, H. Van Lintel, P. Renaud, and M. Gauthier, "Impedance-based real-time position sensor for lab-on-a-chip devices," *Lab Chip*, vol. 18, p. 818, 2018.
- [9] S. Gabriel, R. W. Lau, and C. Gabriel, "The dielectric properties of biological tissues: II. Measurements in the frequency range 10 Hz to 20 GHz," *Phys. Med. Biol.*, vol. 41, p. 2251, 1996.
- [10] A. P. O'Rourke, M. Lazebnik, J. M. Bertram, et al., "Dielectric properties of human normal, malignant and cirrhotic liver tissue: in vivo and ex vivo measurements from 0.5 to 20 GHz using a precision open-ended coaxial probe," *Phys. Med. Biol.*, vol. 52, p. 4707, 2007.
- [11] L. Abdilla, C. Sammut, and L. Z. Mangion, "Dielectric properties of muscle and liver from 500MHz to 40GHz," *Electromagn. Biol. Med.*, vol. 32, pp. 244–252, 2013.
- [12] S. Egot-Lemaire, J. Pijanka, J. Sulé-Suso, and S. Semenov, "Dielectric spectroscopy of normal and malignant human lung cells at ultra-high frequencies," *Phys. Med. Biol.*, vol. 54, p. 2341, 2009.
- [13] M. Al Ahmad, Z. Al Natour, F. Mustafa, and T. A. Rizvi, "Electrical characterization of normal and cancer cells," *IEEE Access*, vol. 6, p. 25979, 2018.
- [14] X. Liang, K. A. Graham, A. C. Johannessen, D. E. Costea, and F. H. Labeed, "Human oral cancer cells with increasing tumorigenic abilities exhibit higher effective membrane capacitance," *Integr. Biol.*, vol. 6, p. 545, 2014.
- [15] H. A. Svahn and A. Van Den Berg, "Single cells or large populations," *Lab Chip*, vol. 7, pp. 544–546, 2007.
- [16] H. E. Ayliffe, A. B. Frazier, and R. D. Rabbitt, "Electrical impedance spectroscopy using microchannels with integrated metal electrodes," *IEEE J. Microelectromech. Syst.*, vol. 8, pp. 50–57, 1999.
- [17] D. K. Wood, S. H. Oh, S. H. Lee, H. T. Soh, and A. N. Cleland, "High-bandwidth radio frequency Coulter counter," *Appl. Phys. Lett.*, vol. 87, p. 184106, 2005.
- [18] D. K. Wood, M. V. Requa, and A. N. Cleland, "Microfabricated high-throughput electronic particle detector," *Rev. Sci. Instrum.*, vol. 78, p. 104301, 2007.
- [19] T. Sun, S. Gawad, C. Bernabini, N. G. Green, and H. Morgan, "Broadband single cell impedance spectroscopy using maximum length sequences: theoretical analysis and practical considerations," *Meas. Sci. Technol.*, vol. 18, p. 2859, 2007.
- [20] T. Sun, C. Bernabini, and H. Morgan, "Single-colloidal particle impedance spectroscopy: complete equivalent circuit analysis of polyelectrolyte microcapsules," *Langmuir*, vol. 26, p. 3821, 2010.
- [21] K. Heileman, J. Daoud, and M. Tabrizian, "Dielectric spectroscopy as a viable biosensing tool for cell and tissue characterization and analysis," *Biosens. Bioelectron.*, vol. 49, pp. 348–349, 2013.
- [22] A. Bhat, J. Rodriguez, H. Qin, et al., "High bandwidth resonant radio frequency circuit for lipid bilayer detection," *Biophys. J.*, vol. 102, p. 181a, 2012.
- [23] A. Bhat, J. Rodriguez, H. Qin, et al., "Radio frequency tank circuit for probing planar lipid bilayers," *Soft Nanosci. Lett.*, vol. 03, p. 87, 2013.
- [24] E. Stava, H. C. Shin, M. Yu, et al., "Ultra-stable glass microcraters for on-chip patch clamping," *RSC Adv.*, vol. 4, p. 39073, 2014.

- [25] P. J. Resto, A. Bhat, E. Stava, et al., “Flow characterization and patch clamp dose responses using jet microfluidics in a tubeless microfluidic device,” *J. Neurosci. Methods*, vol. 291, p. 182, 2017.
- [26] F. Artis, T. Chen, T. Chretiennot, et al., “Microwaving biological cells: intracellular analysis with microwave dielectric spectroscopy,” *IEEE Microw. Mag.*, vol. 16, p. 87, 2015.
- [27] J. Chen, C. Xue, Y. Zhao, D. Chen, M. H. Wu, and J. Wang, “Microfluidic impedance flow cytometry enabling high-throughput single-cell electrical property characterization,” *Int. J. Mol. Sci.*, vol. 16, pp. 9804–9830, 2015.
- [28] C. S. Bausch, C. Heyn, W. Hansen, et al., “Ultra-fast cell counters based on microtubular waveguides,” *Sci. Rep.*, vol. 7, pp. 41584–41592, 2017.
- [29] M. Yu, H.-S. Kim, and R. H. Blick, “Laser drilling of nano-pores in sandwiched thin glass membranes,” *Opt. Express*, vol. 17, p. 10044, 2009.
- [30] J. Rodriguez, H.-C. Shin, E. Stava, et al., “Ablating nanoscale pores in crystalline quartz using laser-induced micro-plasmas in tri-layer structures,” *Opt. Mater. Express*, vol. 10, p. 1991, 2020.
- [31] A. Bhat, P. V. Gwozdz, A. Seshadri, M. Hoeft, and R. H. Blick, “Tank circuit for ultrafast single-particle detection in micropores,” *Phys. Rev. Lett.*, vol. 121, 2018, <https://doi.org/10.1103/PhysRevLett.121.078102>.
- [32] T. Tao, J. Ro, and J. Melngailis, “Focused ion beam induced deposition of platinum,” *J. Vac. Sci. Technol. B Microelectron. Nanom. Struct.*, vol. 8, pp. 1826–1829, 1990.
- [33] G. J. Verbiest and M. J. Rost, “Beating beats mixing in heterodyne detection schemes,” *Nat. Commun.*, vol. 6, 2015, <https://doi.org/10.1038/ncomms7444>.
- [34] H. Happy, K. Haddadi, D. Theron, T. Lasri, and G. Dambrine, “Measurement techniques for RF nanoelectronic devices: new equipment to overcome the problems of impedance and scale mismatch,” *IEEE Microw. Mag.*, vol. 15, p. 30, 2014.
- [35] V. T. Rathod, “A review of electric impedance matching techniques for piezoelectric sensors, actuators, and transducers,” *Electron*, vol. 8, p. 169, 2019.
- [36] R. M. M. Smeets, U. F. Keyser, N. H. Dekker, and C. Dekker, “Noise in solid-state nanopores,” *Proc. Natl. Acad. Sci. U. S. A.*, vol. 105, p. 417, 2008.
- [37] J. K. Rosenstein, M. Wanunu, C. A. Merchant, M. Drndic, and K. L. Shepard, “Integrated nanopore sensing platform with sub-microsecond temporal resolution,” *Nat. Methods*, vol. 9, p. 487, 2012.
- [38] J. Harberts, R. Zierold, C. Fendler, et al., “Culturing and patch clamping of Jurkat T cells and neurons on Al₂O₃ coated nanowire arrays of altered morphology,” *RSC Adv.*, vol. 9, p. 11194, 2019.
- [39] J. Harberts, M. Kusch, J. O’sullivan, R. Zierold, and R. H. Blick, “A temperature-controlled patch clamp platform demonstrated on Jurkat T lymphocytes and human induced pluripotent stem cell-derived neurons,” *Bioengineering*, vol. 7, p. 46, 2020.
- [40] S. Elmore, “A review of programmed cell death,” *Toxicol. Pathol.*, vol. 35, pp. 495–516, 2007.